SCIENCE CHINA
Physics, Mechanics & Astronomy

•Article•
Special Topic: The Chinese Hα Solar Explorer—CHASE Mission

August 2022 Vol. 65 No. 8: 289605
https://doi.org/10.1007/s11433-022-1917-1

On the technologies of Hα imaging spectrograph for the CHASE mission

Qiang Liu[1*], Hongjiang Tao[1], Changzheng Chen[1], Chengshan Han[1*], Zhe Chen[1], Gui Mei[1], Liang Yang[1], Qinglong Hu[1], Hongwei Xin[1], Xiansheng Li[1], Hongyu Guan[1], Donglin Xue[1], Mingchao Zhu[1], Changhong Hu[1], Qinghua Ha[1], Yukun He[1], Cheng Fang[2,3], Chuan Li[2,3], and Zhen Li[2,3]

[1] *Changchun Institute of Optics, Fine Mechanics and Physics, Chinese Academy of Sciences, Changchun 130033, China;*
[2] *School of Astronomy and Space Science, Nanjing University, Nanjing 210023, China;*
[3] *Key Laboratory for Modern Astronomy and Astrophysics, Ministry of Education, Nanjing 210023, China*

Received March 31, 2022; accepted April 24, 2022; published online July 5, 2022

The Hα imaging spectrograph (HIS) is the scientific payload of the first solar space mission, the Chinese Hα solar explorer (CHASE), supported by the China National Space Administration (CNSA). The CHASE/HIS achieves, for the first time in space, Hα spectroscopic observations with high spectral and temporal resolutions. Separate channels for the raster scanning mode (RSM) and continuum imaging mode (CIM) are integrated into one, and a highly integrated design is achieved through multiple folding of the optical path and ultra-light miniaturized components. The design of HIS implements a number of key technologies such as high-precision scanning of the optical field of view (FOV), high-precision integrated manufacturing inspection, a large-tolerance pre-filter window, and full-link solar radiation calibration. The HIS instrument has a pixel spectral resolution of 0.024 Å and can complete a full-Sun scanning within 46 s.

space-based telescope, design and performance testing of optical systems, scan imaging

PACS number(s): 95.55.Fw, 42.82.Bq, 42.79.Ls

Citation: Q. Liu, H. Tao, C. Chen, C. Han, Z. Chen, G. Mei, L. Yang, Q. Hu, H. Xin, X. Li, H. Guan, D. Xue, M. Zhu, C. Hu, Q. Ha, Y. He, C. Fang, C. Li, and Z. Li, On the technologies of Hα imaging spectrograph for the CHASE mission, Sci. China-Phys. Mech. Astron. **65**, 289605 (2022), https://doi.org/10.1007/s11433-022-1917-1

1 Introduction

The Sun is the only star that can be observed with high spectral and spatial resolutions. It is a natural laboratory for humans to understand other stars, as well as the Universe. In addition, solar activity and its impact on the solar-terrestrial space environment are the main objectives of space weather forecasting. Therefore, observation of, and research into, solar activity has both scientific and practical significance.

The first solar Hα images were obtained by Hale [1] at the Mount Wilson Solar Observatory. Since then, Hα spectroscopic observations have been carried out with ground-based telescopes [2-6]. The solar dynamic Doppler imager (SDDI) installed at Hida Observatory in Japan can observe full-Sun Hα images [7]. SDDI uses a tunable filter to obtain Hα images with a spectral resolution of 0.25 Å. The interfacial imaging spectrograph (IRIS), launched by the United States in 2013, operates in a Sun-synchronous orbit, mainly for

*Corresponding authors (Qiang Liu, email: liudequ@126.com; Chengshan Han, email: han_chengshan@163.com)

observations in the ultraviolet waveband [8]. Unlike previous solar satellites that mainly observed the upper solar corona through ultraviolet and X-rays [9,10], the Hα imaging spectrograph (HIS) specializes in observing the lower solar atmosphere, namely the photosphere and chromosphere [11-13]. As a solar spectrograph in space, it has advantages compared to ground-based observations [14,15]. First, due to the seeing effects arising from the Earth's atmosphere, the spatial resolution of ground-based telescopes cannot easily reach the designed resolution except when using adaptive optics systems. Second, the spectrograph in orbit can realize all-day and all-weather observations, which is well matched with the observations of other space telescopes in other bands, e.g., the to-be-launched Advanced Space-based Solar Observatory (ASO-S) [16]. As such, we can conduct a comprehensive study of all levels of the solar atmosphere and fully understand the evolution process and physical mechanism of solar activity.

At 18:51 on October 14, 2021, China successfully launched its first solar space mission—the Chinese Hα Solar Explorer (CHASE)—at the Taiyuan Satellite Launch Center. The HIS instrument is the scientific payload of the CHASE mission. It achieves, for the first time in space, solar Hα spectroscopic observation with high spectral and temporal resolutions [17-19]. In this paper, we present detailed descriptions of the HIS instrument, including its optical systems, mechanics, and electronics.

2 Composition of the HIS instrument

The HIS instrument includes a filter window part, an optical system part, a thermal control part, and a focusing apparatus. Figure 1 shows the composition of the HIS instrument. In terms of structural composition, the HIS instrument consists of two parts: the filter window assembly and the imaging spectrograph body. The filter window assembly is composed of two optical mirrors, which can shield most wavelengths of sunlight to prevent overheating inside the camera. The light beam from the Sun first enters the HIS instrument through the filter window and passes through the front off-axis three-mirror optical system. The beam splitter at the exit pupil of the system splits the light, and part of the light path enters the off-axis three-mirror imaging system and passes through a narrow-band filter on the continuum imaging mode (CIM) unit. The capture rate is 1 fps, and the pixel array is 5120 × 5120. Another channel of sunlight enters the raster scanning mode (RSM) unit and passes through the telecentric optical system, scanning drive mechanism, slit, plane grating, collimating mirror, and imaging mirror, so that the two-dimensional spectral scanning image of the Sun is produced on the spectral scanning imaging focal plane. The imaging frame rate is 100 fps, the slit width is 9 μm, the line density of the plane grating is 1900 lp/mm (first-order diffracted light is used), and the center wavelength is 6562.81 Å. The pixel size of the detector is 4.6 μm, the pixel spectral re-

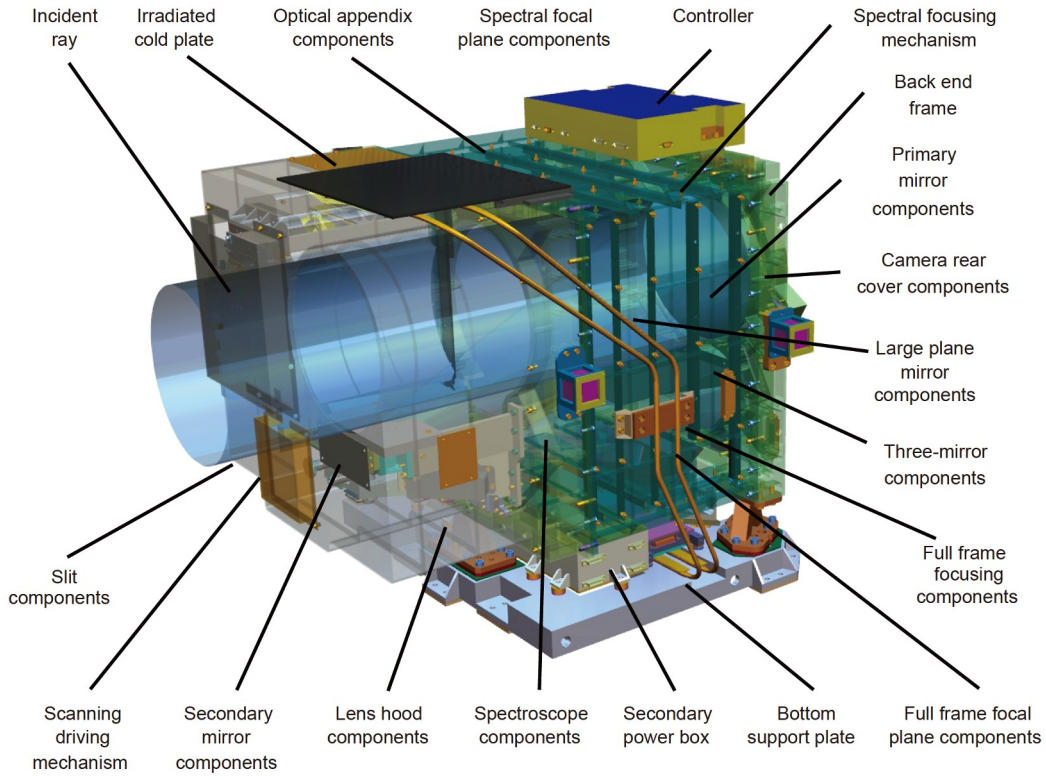

Figure 1 Composition of the HIS instrument.

solution is 0.024 Å, and the instrument FWHM is 0.072 Å. After the compression unit compresses the image data, the compressed code stream is sent to the data transmission satellite through the LVDS interface. Figure 2 shows the operational diagram of the HIS instrument.

The front three-mirror-anastigmatic (TMA) optical system of the HIS instrument has an intermediate image plane and an available real exit pupil, which is convenient for the suppression of stray light and the connection with each subsystem. It has wide field of view (FOV) and long focal length [14,20]. The mass of the HIS instrument is 54.9 kg, the size is 635 mm × 556 mm × 582 mm, the focal length is 1820 mm, the diameter is Φ180 mm, F number is 10.1, and the FOV is 40′ × 40′. Table 1 surveys the parameters of the HIS instrument. Table 2 shows the RSM channel parameters. See Table 3 for the CIM channel parameters.

Table 1 Specifications of the HIS instrument

Item	Parameter
Volume	635 mm × 556 mm × 582 mm
Weight	54.9 kg
Power	average 58 W, peak 98 W
Focal length	1820 mm
Aperture	180 mm
Field of view	40′ × 40′

Table 2 RSM channel parameters

Item	Parameter
Observation spectrum	Hα: 6559.7-6565.9 Å, FeI: 6567.8-6570.6 Å
Line half width (FWHM)	0.072 Å
Field of view	40′ × 40′
Pixel resolution	0.52″
Time resolution	46 s
Pixel spectral resolution	0.024 Å
Image quantization bits	12 bit
SNR	20.3 db
Laboratory absolute radiometric calibration accuracy	better than 5%
Relative radiometric calibration accuracy	better than 3%
Image data compression ratio	6:1

3 Technologies of HIS instrument

3.1 High-precision scan imaging method

The main design idea of spectral scan imaging is to set a slit at the image plane of the telecentric optical system on the front image side. The light enters the spectral scan imaging unit after passing through the slit, and the slit images of different wavelengths are spread along the direction perpendicular to the slit, producing images at the focal plane of the spectral scan imaging unit. The hyperspectral image can be obtained by signal extraction and spectrograph image processing. Considering the balance of energy and resolution, a slit width of 9 μm was adopted. Figure 3 shows the

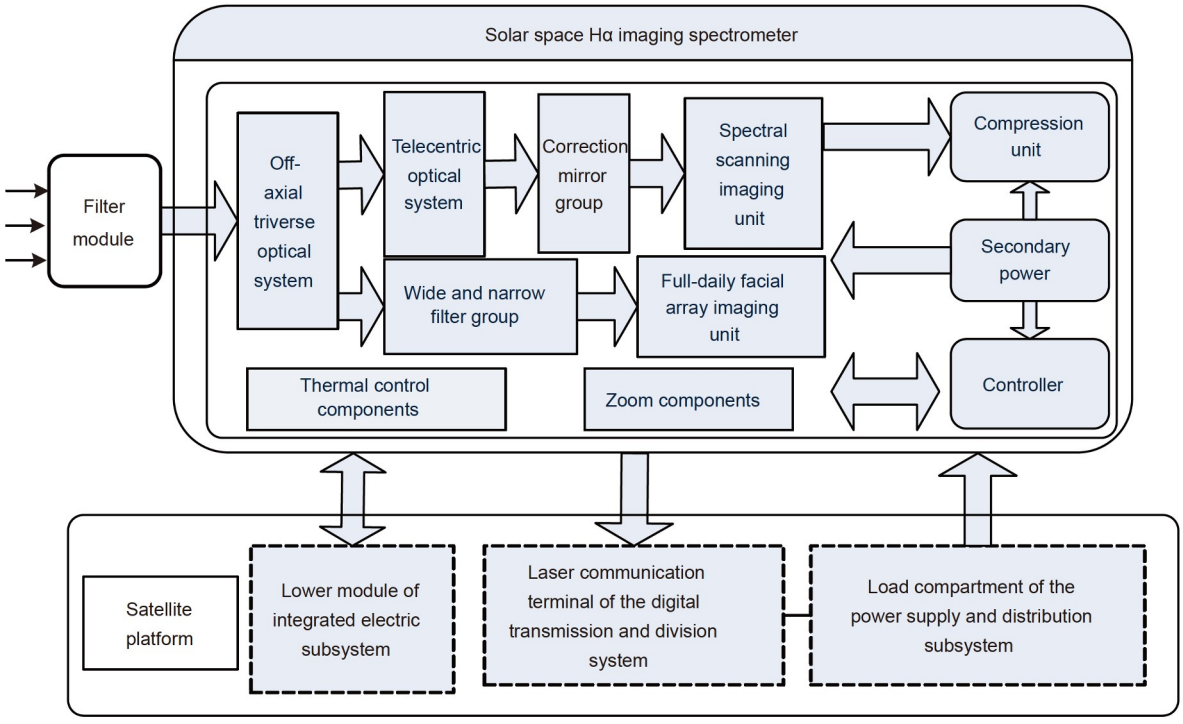

Figure 2 Operational diagram of the Hα imaging spectrograph.

Table 3 CIM channel parameters

Item	Parameter
Center wavelength	6689 Å
FWHM	13.4 Å
Field of view	40′ × 40′
Pixel resolution	0.52″
Highest frame rate	1 fps
Image quantization bits	10 bit
Static MTF	≥0.25 (@55 lp/mm)
Laboratory absolute radiometric calibration accuracy	better than 5%
Relative radiometric calibration accuracy	better than 3%
SNR	20.2 db
Image data compression ratio	6:1

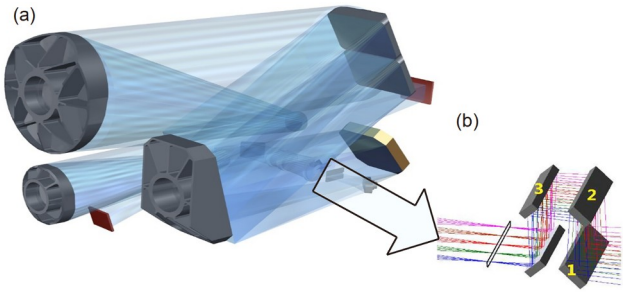

Figure 3 Schematic diagram of optical field scan imaging. (a) Optical system; (b) mirror field of view scan sequence.

schematic diagram for the optical field scan imaging.

To achieve spectral observation of the entire solar surface, it is necessary to scan the FOV perpendicular to the slit direction, as shown in Figure 3(b). Thus, one sets up fast and slow mirror groups in front of the slit; in Figure 3(b), the fast mirror group is labeled 3, and the slow mirror groups are 1 and 2. Through the movement of the fast and slow mirror groups, optical field view scanning in the direction of the vertical slit can be achieved, while the rest of the system remains stationary. During scanning, the linear motor drives the fast mirror group to reciprocate up and down at a speed V; at the same time, the slow mirror group moves up and down at $0.5V$, so that the image plane of the front-end optical system can be scanned and imaged. Full solar imaging is achieved by the movement of the optical element, which is different from the birefringent filter scheme used in ground observation. This scheme has lower requirements for motion accuracy, and the motion error does not affect the spectral resolution. It also has good environmental adaptability, stable output, and high reliability.

Through the high-precision scanning optical field imaging method, the two-dimensional spectral image of the Sun is obtained provided the satellite and the camera remain stationary, and the full-Sun scanning of the solar spectra is completed within 46 s.

3.2 High-precision dual-motor synchronous scanning technology

In the development process, to achieve high precision and synchronized movement of the fast and slow mirror groups, a highly integrated spectral scanning mechanism is designed to carry the fast and slow mirror groups and implement the synchronous scanning function. The spectral scanning mechanism is arranged between the slit and the correction mirror. In a compact space of only 22 mm along the optical path, the spectral scanning mechanism implements the high-precision driving, high-sensitivity position feedback, and high-reliability mechanism locking functions of the two mirror groups. Figure 4 shows the composition of the scanning mechanism.

The fast and slow mirror groups of the driving mechanism are separately controlled by linear motors, and the control accuracy of the dual motors is improved by adopting a variety of software control methods [21-23], starting with FPGA implementing complex planning and two-degree-of-freedom control algorithms. There is also a torque observer to compensate for external disturbances, which achieves a dynamic tracking accuracy of 0.2 μm, and we obtain significantly improved positioning accuracy through kinematic calibration. The specific implementation is shown in Figure 5.

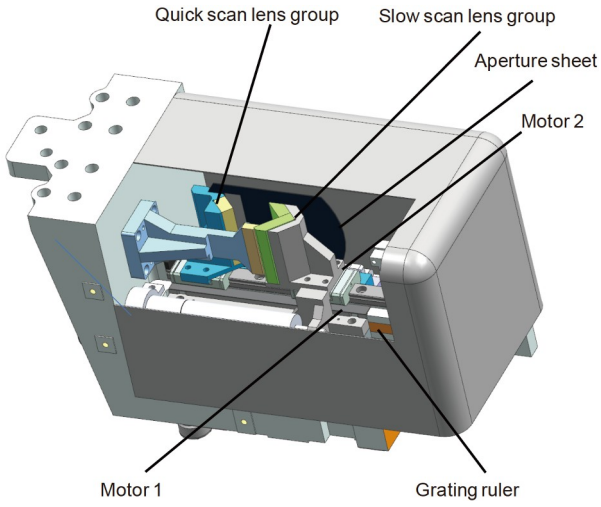

Figure 4 Composition of the scanning mechanism.

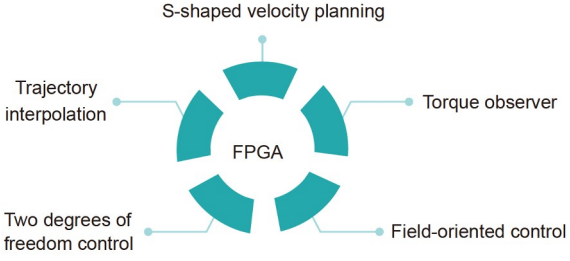

Figure 5 Motor speed control method.

The linear motors, linear guides, and grating scales of the two mirror groups of the driving mechanism adopt a common reference design and adjustment method, and the high-precision real-time synchronization of the two moving mirror groups is implemented through the above-mentioned high-precision voice coil motor driving and trajectory control technology. Accuracy tests verify that the absolute position deviation of the two moving mirror groups is better than 9 μm, the speed stability of the fast scan mirror group is better than ±0.3 μm/10 ms, and the speed stability of the slow scan mirror group is better than ±0.2 μm/10 ms. The speed stability test results of the fast and slow scan motors are shown in Figures 6 and 7, respectively. It is better than the technical requirements that the absolute position deviation of the two mirror groups is 10 μm and the speed stability is ±1 μm/10 ms.

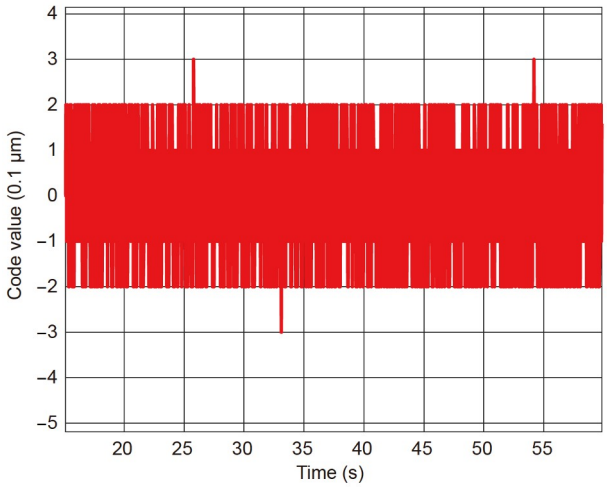

Figure 6 Fast scan motor speed accuracy test results.

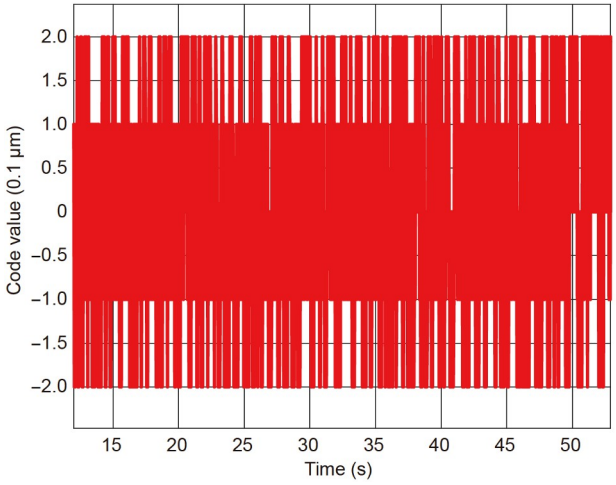

Figure 7 Slow scan motor speed accuracy test results.

3.3 High-precision integrated manufacturing and testing technology

The solar Hα imaging spectrograph integrates two channels of RSM and CIM. There are many optical elements and motion mechanisms inside, requiring 2 sets of optical systems, 2 focal planes, 3 sets of motion mechanisms, 17 optical lenses, and 32 components, integrated within a space of 610 mm × 550 mm × 500 mm. Thus, optical assembly and integration are extremely difficult. The R&D team adopted a series of innovative methods to solve the optical and structural problems and achieve a pixel spectral resolution of 0.024 Å.

As shown in Figure 8, the solar Hα imaging spectrograph adopts the variable wavelength rotating interference imaging method to complete the precise adjustment of the spectroscopic system during optical adjustment, which solves the problem of inconsistency between the detection wavelength of the interferometer and the working wavelength of the system. Thus, the image quality of the spectrograph reaches the diffraction limit. At the same time, the common reference computational hologram (CGH) detection technology is adopted [24,25], which greatly reduces the degree of freedom of each mirror, and completes the rapid positioning and adjustment of multiple off-axis aspheric mirrors [26,27], which is 30% more efficient than the traditional method.

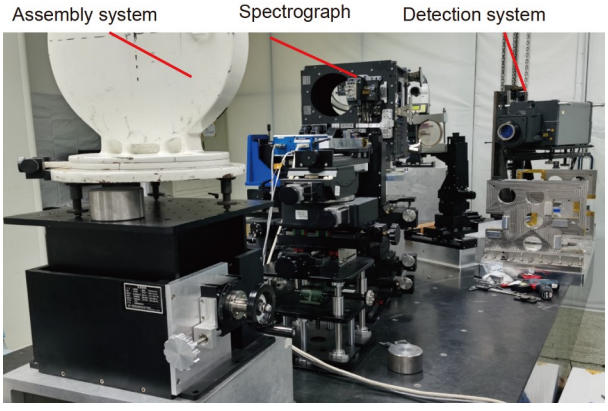

Figure 8 Integration and detection system.

3.4 Large tolerance pre-filter window technology

A filter window is set at the front end of the solar space Hα spectrograph. Its functions include band-pass filtering, preventing ultraviolet and infrared rays from entering the optical system, and preventing radiation damage. The filter assembly adopts a two-layer structure, comprising a radiation-proof glass and a sapphire glass. The lens is coated with both a band-pass film and an infrared cutoff film. Through spectral optimization, most wavelengths of sunlight can be blocked to prevent overheating inside the camera. The aperture of the filter window is 200 mm, which ensures that

the FOV of sunlight entering the optical system meets the system requirements. Figure 9 shows a schematic diagram of the filter window.

The filter window is located outside the satellite cabin and is exposed to the cool and dark space, and the optical lens is exposed to direct sunlight. One requires high surface shape accuracy of the optical lens under large temperature differences (RMS value is better than 12 nm), which introduces some difficulties to the design. We achieved large-tolerance adaptability of the filter window by adopting the flexible support design of dual optical mirrors to match the on-orbit high-temperature stress release design and assembly method [28-30]. We adopt large-tolerance pre-filter window technology, multiple narrow-band filters (bandwidth 1 nm) and high-contrast (5000:1) optical attenuation technology to accurately locate the observation wavelength. The central wavelength of the finally realized observation spectrum is 6689 Å, and the bandwidth is 13 Å, which meets the requirement that the index central wavelength is 6689 Å and the bandwidth is not greater than 30 Å.

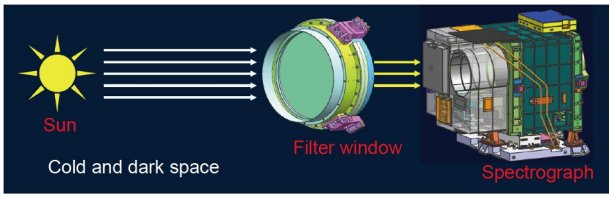

Figure 9 Operational diagram of the filter window.

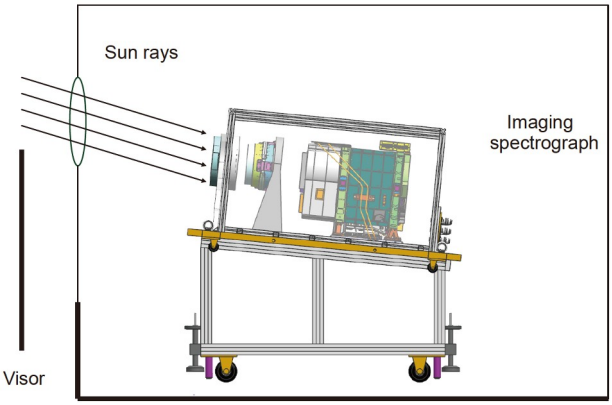

Figure 10 Schematic view of the imaging experiment.

3.5 Full-link solar radiation calibration technology

The solar radiance is 1×10^5 times the radiance of the Earth's surface, and laboratory light sources do not provide the conditions for radiometric calibration. Therefore, a full-link solar radiation calibration system was designed, and the calibration was completed through field imaging experiments.

The field imaging experiment was carried out by using a heliostat to introduce sunlight into the camera in the laboratory. The first mirror automatically adjusts the angular position in real time according to the Sun's trajectory (azimuth and altitude), and reflects the sunlight to the secondary mirror, which reflects the sunlight into the laboratory.

After the sunlight is introduced into the laboratory calibration system through the light entrance on the window through the heliostat, as shown in Figure 10, the solar telescope receives the sunlight and starts the imaging experiment. To prevent the grating of the solar telescope from being affected by fine dust in the environment, the solar telescope is placed in a clean airtight cabin. In the testing process of the solar telescope, a spectroradiometer is used to test the irradiance incident into the solar telescope, and the shading plate is used to shield the sunlight to test the irradiance of the background light in the laboratory.

The field calibration test includes a full solar imaging test and spectral scan imaging test. In the full-disk imaging test, the determination of the integration time of the full-disk on-orbit work, the calibration of the integral time relationship, the flat-field calibration, the laboratory absolute radiation calibration, and the laboratory relative radiation calibration were carried out. The linear fitting degree of the output gray value relationship is 0.9999, the laboratory absolute radiation calibration accuracy is better than 3.5% (the index requirement is better than 5%), and the laboratory relative radiation calibration accuracy is better than 2.7% (the index requirement is better than 3%). In the spectral scanning imaging test, the integration time and spectral line position determination, integration time relationship calibration, scanning imaging function test, laboratory absolute radiometric calibration, and laboratory relative radiometric calibration were carried out. The linear fitting degree of the gray value relationship is 0.9999, the laboratory absolute radiation calibration accuracy is better than 4.2% (the index requirement is better than 5%), and the laboratory relative radiation calibration accuracy is better than 2.5% (the index requirement is better than 3%).

By establishing a full-link solar radiation calibration system, equivalent to on-orbit solar imaging, the imaging function and performance of the solar imaging spectrograph were comprehensively tested, and the on-orbit operating parameters of the imaging spectrograph were determined.

3.6 High frame rate dynamic imaging technology

When the solar space Hα spectrograph is on-orbit imaging, it needs to achieve the goals of a high frame rate and high data rate via an extremely high single lane rate, which leads to the reduction in the data time margin; data jitter and reception stability also directly affect the image quality. At the same time, it also needs to consider the on-orbit imaging time; the

shortest, continuous imaging time of the spectrograph on-orbit is 20 min and the longest is 10 h. Therefore, the imaging process must consider the thermal noise from devices and circuits caused by temperature changes.

To solve the above problems, dynamic phase detector technology is introduced. During the serial-to-parallel conversion process, the data phase offset detection is carried out. After the offset is found, the output sampling window position is moved in real time, and the rising edge of the control clock is aligned with the center position of the data window to ensure data stability. After completing the 100 fps strip window dynamic imaging driver, testing shows that the image is clear, the contrast is high, and the frame rate stability is better than 100 pps.

In addition, through functional optimization and integration, the integration level is improved, and the real-time compression of high-speed dynamic imaging data is achieved in a limited space. The data processing data rate is greater than 2.2 Gbps, which is equivalent to a data volume of an optical camera with a width of 150 km and a resolution of 2 m.

4 Conclusion

The main payload of CHASE is the HIS instrument designed based on the off-axis TMA optical system and spectral scan imaging technology. It marks the on-orbit application of the world's first HIS instrument and has achieved space observation of the solar Hα band with high spectral resolution. By adopting a series of innovative technologies, such as the high-precision scan imaging method, high-precision integrated manufacturing detection technology, large-tolerance pre-filter window technology, full-link solar radiation calibration technology, and high frame rate dynamic imaging technology, we have guaranteed that this solar Hα imaging spectrograph can achieve a pixel spectral resolution of 0.024 Å, and can complete a full solar surface scan of the solar spectrum within 46 s. Both spectral resolution and temporal resolution are competitive on an international level.

The CHASE mission was supported by the China National Space Administration (CNSA).

1 G. E. Hale, *Contributions from the Mount Wilson Observatory* (Carnegie Institution, Washington, 1908).
2 Z. Liu, J. Xu, B. Z. Gu, S. Wang, J. Q. You, L. X. Shen, R. W. Lu, Z. Y. Jin, L. F. Chen, K. Lou, Z. Li, G. Q. Liu, Z. Xu, C. H. Rao, Q. Q. Hu, R. F. Li, H. W. Fu, F. Wang, M. X. Bao, M. C. Wu, and B. R. Zhang, Res. Astron. Astrophys. **14**, 705 (2014).
3 W. Pötzi, A. M. Veronig, M. Temmer, D. J. Baumgartner, H. Freislich, and H. Strutzmann, Sol. Phys. **291**, 3103 (2016), arXiv: 1512.00270.
4 C. Fang, B. Z. Gu, X. Y. Yuan, M. D. Ding, P. F. Chen, Z. G. Dai, X. D. Li, Y. Shi, J. W. Xie, J. M. Bai, Z. Q. Qu, Q. Hao, Y. Quo, X. Cheng, and Z. Li, Sci. Sin.-Phys. Mech. Astron. **49**, 059603 (2019).
5 C. H. Rao, N. T. Gu, X. J. Rao, C. Li, L. Q. Zhang, J. L. Huang, L. Kong, M. Zhang, Y. T. Cheng, Y. Pu, H. Bao, Y. M. Guo, Y. Y. Liu, J. S. Yang, L. B. Zhong, C. J. Wang, K. Fang, X. J. Zhang, D. H. Chen, C. Wang, X. L. Fan, Z. W. Yan, K. L. Chen, X. Y. Wei, L. Zhu, H. Liu, Y. J. Wan, H. Xian, and W. L. Ma, Sci. China-Phys. Mech. Astron. **63**, 109631 (2020).
6 X. L. Yan, Z. Liu, J. Zhang, and Z. Xu, Sci. China Tech. Sci. **63**, 1656 (2020), arXiv: 1910.09127.
7 K. Ichimoto, T. T. Ishii, K. Otsuji, G. Kimura, Y. Nakatani, N. Kaneda, S. I. Nagata, S. UeNo, K. Hirose, D. Cabezas, and S. Morita, Sol. Phys. **292**, 63 (2017).
8 B. de Pontieu, A. M. Title, J. R. Lemen, G. D. Kushner, D. J. Akin, B. Allard, T. Berger, P. Boerner, M. Cheung, C. Chou, J. F. Drake, D. W. Duncan, S. Freeland, G. F. Heyman, C. Hoffman, N. E. Hurlburt, R. W. Lindgren, D. Mathur, R. Rehse, D. Sabolish, R. Seguin, C. J. Schrijver, T. D. Tarbell, J. P. Wülser, C. J. Wolfson, C. Yanari, J. Mudge, N. Nguyen-Phuc, R. Timmons, R. van Bezooijen, I. Weingrod, R. Brookner, G. Butcher, B. Dougherty, J. Eder, V. Knagenhjelm, S. Larsen, D. Mansir, L. Phan, P. Boyle, P. N. Cheimets, E. E. DeLuca, L. Golub, R. Gates, E. Hertz, S. McKillop, S. Park, T. Perry, W. A. Podgorski, K. Reeves, S. Saar, P. Testa, H. Tian, M. Weber, C. Dunn, S. Eccles, S. A. Jaeggli, C. C. Kankelborg, K. Mashburn, N. Pust, L. Springer, R. Carvalho, L. Kleint, J. Marmie, E. Mazmanian, T. M. D. Pereira, S. Sawyer, J. Strong, S. P. Worden, M. Carlsson, V. H. Hansteen, J. Leenaarts, M. Wiesmann, J. Aloise, K. C. Chu, R. I. Bush, P. H. Scherrer, P. Brekke, J. Martinez-Sykora, B. W. Lites, S. W. McIntosh, H. Uitenbroek, T. J. Okamoto, M. A. Gummin, G. Auker, P. Jerram, P. Pool, and N. Waltham, Sol. Phys. **289**, 2733 (2014), arXiv: 1401.2491.
9 Y. G. Xing, L. Li, J. Peng, S. S. Wang, and Y. N. Cheng, Acta Opt. Sin. **41**, 0730003 (2021).
10 J. L. Peng, T. J. Feng, X. Y. Nie, D. B. Tian, Z. Yi, S. S. Wang, Q. Yu, K. Zhang, and Z. L. Ma, Spectrosco. Spectr. Anal. **39**, 953 (2019).
11 C. Fang, P. F. Chen, Z. Li, M. D. Ding, Y. Dai, X. Y. Zhang, W. J. Mao, J. P. Zhang, T. Li, Y. J. Liang, and H. T. Lu, Res. Astron. Astrophys. **13**, 1509 (2013), arXiv: 1307.4533.
12 P. F. Chen, Sci. China-Phys. Mech. Astron. **61**, 109631 (2018).
13 C. Li, C. Fang, Z. Li, M. D. Ding, P. F. Chen, Z. Chen, L. K. Lin, C. Z. Chen, C. Y. Chen, H. J. Tao, W. You, Q. Hao, Y. Dai, X. Cheng, Y. Guo, J. Hong, M. J. An, W. Q. Cheng, J. X. Chen, W. Wang, and W. Zhang, Res. Astron. Astrophys. **19**, 165 (2019).
14 R. Z. Ma, C. L. Wang, C. Z. Chen, Z. Chen, and Y. Jia, Sci. Sin.-Phys. Mech. Astron. **50**, 049601 (2020).
15 Z. P. Cai, X. X. Zhang, Z. Chen, and G. L. Bi, Chin. J. Liquid Cryst. Displays **35**, 845 (2020).
16 W. Q. Gan, C. Zhu, Y. Y. Deng, H. Li, Y. Su, H. Y. Zhang, B. Chen, Z. Zhang, J. Wu, L. Deng, Y. Huang, J. F. Yang, J. J. Cui, J. Chang, C. Wang, J. Wu, Z. S. Yin, W. Chen, C. Fang, Y. H. Yan, J. Lin, W. M. Xiong, B. Chen, H. C. Bao, C. X. Cao, Y. P. Bai, T. Wang, B. L. Chen, X. Y. Li, Y. Zhang, L. Feng, J. T. Su, Y. Li, W. Chen, Y. P. Li, Y. N. Su, H. Y. Wu, M. Gu, L. Huang, and X. J. Tang, Res. Astron. Astrophys. **19**, 156 (2019).
17 C. Li, C. Fang, Z. Li, M. D. Ding, P. F. Chen, Y. Qiu, W. You, Y. Yuan, M. J. An, H. J. Tao, X. S. Li, Z. Chen, Q. Liu, G. Mei, L. Yang, W. Zhang, W. Q. Cheng, J. X. Chen, C. Y. Chen, Q. Gu, Q. L. Huang, M. X. Liu, C. S. Han, H. W. Xin, C. Z. Chen, Y. W. Ni, W. B. Wang, S. H. Rao, H. T. Li, X. Lu, W. Wang, J. Lin, Y. X. Jiang, L. J. Meng, and J. Zhao, Sci. China-Phys. Mech. Astron. **65**, 289602 (2022).
18 Y. Qiu, S. H. Rao, C. Li, C. Fang, M. D. Ding, Z. Li, Y. W. Ni, W. B. Wang, J. Hong, Q. Hao, Y. Dai, P. F. Chen, X. S. Wan, Z. Xu, W. You, Y. Yuan, H. J. Tao, X. S. Li, Y. K. He, and Q. Liu, Sci. China-Phys. Mech. Astron. **65**, 289603 (2022).
19 W. Zhang, W. Q. Cheng, W. You, X. Chen, J. Zhang, C. Li, and C. Fang, Sci. China-Phys. Mech. Astron. **65**, 289604 (2022).
20 Z. Chen, X. X. Zhang, C. Z. Chen, and J. Y. Ren, Chin. J. Laser **43**, 0416002 (2016).
21 B. Ahi, and A. Nobakhti, IEEE Trans. Contr. Syst. Technol. **26**, 2268

(2018).
22 J. S. Lee, S. Y. Lim, I. Kim, W. Jeong, S. Won, and H. Yang, IEEE Trans. Mag. **53**, 8000409 (2017).
23 L. Wang, J. Su, and G. Xiang, IEEE Trans. Ind. Electron. **63**, 6519 (2016).
24 F. Z. Li, X. Luo, J. L. Zhao, D. L. Xue, L. G. Zheng, and X. J. Zhang, Opti. Precis. Eng. **19**, 709 (2011).
25 S. T. Gao, Y. X. Sui, and H. J. Yang, Acta Opt. Sin. **33**, 0612003 (2013).
26 Q. Cheng, and D. L. Xue, Acta Opt. Sin. **7**, 123 (2016).
27 D. Su, E. Miao, Y. Sui, and H. Yang, Opt. Lett. **37**, 3198 (2012).
28 P. R. Yoder, and D. Vukobratovich, *Opto-Mechanical Systems Design* (CRC Press, Boca Raton, 2020), p. 708.
29 F. Maamar, and A. Boudjemai, Adv. Space Res. **65**, 2263 (2020).
30 H. Y. Kihm, H. S. Yang, I. K. Moon, and Y. W. Lee, J. Opt. Soc. Korea **13**, 201 (2009).